

## ARTICLES

## Bicrystalline Hematite Nanowires

Rongming Wang,<sup>\*,†,‡,§</sup> Yaofeng Chen,<sup>†</sup> Yunyi Fu,<sup>†</sup> Han Zhang,<sup>†</sup> and Christian Kisielowski<sup>\*,‡</sup>

State Key Laboratory for Mesoscopic Physics, Department of Physics, Peking University, Beijing 100871, People's Republic of China, and National Center for Electron Microscopy, Lawrence Berkeley National Laboratory, University of California, Berkeley, California 94720

Received: March 8, 2005; In Final Form: April 19, 2005

Bicrystalline nanowires of hematite ( $\alpha$ -Fe<sub>2</sub>O<sub>3</sub>) have been successfully synthesized by the oxidation of pure iron. The product was characterized by X-ray diffraction, scanning electron microscopy, transmission electron microscopy (TEM), high-resolution TEM in combination with focal series reconstruction, energy-dispersive X-ray spectroscopy, and electron energy-loss spectroscopy. The bicrystalline nanowires have diameters of 20–80 nm and lengths up to 20  $\mu$ m. All of the investigated materials are found to be  $\alpha$ -Fe<sub>2</sub>O<sub>3</sub> with a rhombohedral crystal structure. Investigations indicate that most of the bicrystalline nanowires are nanotwins with ellipsoidal heads. The orientation relationship between the nanotwins can be described as  $(\bar{1}110)_M//(\bar{1}110)_T$ ,  $[110]_M/[1\bar{1}0]_T$ . An energy-filtered TEM investigation indicates that the ellipsoidal head is iron-rich. The growth mechanism of such unique nanostructures is considered to be a solid-phase growth via surface and internal diffusions of molecules from base to tip.

## Introduction

Nanotubes, nanowires, and nanobelts are basic functional components for future mechanical, electronic, optical, and optoelectronic nanodevices<sup>1</sup> and have attracted much attention in recent years. A variety of quasi-one-dimensional (1D) nanostructures have been synthesized and have become a research focus for advanced “bottom-up” nanotechnology.<sup>2</sup> Among them, hematite ( $\alpha$ -Fe<sub>2</sub>O<sub>3</sub>), the most stable iron oxide under ambient conditions, is of significant scientific and technological importance due to its excellent properties. It has a small band gap (2.1 eV), high resistivity to corrosion, and low cost. It can, for example, be used as a photoelectrode for solar energy conversion,<sup>3</sup> gas sensors,<sup>4</sup> or heterogeneous catalysts.<sup>5</sup> Recently, bicrystalline nanowires of Si, ZnO, ZnS, and CuO containing a single twin boundary along the entire length of the growth axis were obtained.<sup>6</sup> These unusual structures offer model systems for the study of charge and mass transport along single defects and can serve as templates for novel device structures. However, there is no report on  $\alpha$ -Fe<sub>2</sub>O<sub>3</sub> bicrystalline nanowires. In this paper, we report on the synthesis and characterization of  $\alpha$ -Fe<sub>2</sub>O<sub>3</sub> bicrystalline nanowires by a simple iron oxidation process.

## Experimental Section

The experimental techniques used in the present study are similar to those described previously.<sup>7</sup> Annealed pure iron

( $\geq 99.96$  wt %) substrates ( $5 \times 5 \times 2.5$  mm<sup>3</sup>) were polished, cleaned with alcohol under ultrasonic treatment, and placed in the center of a quartz tube. This tube was inserted into a horizontal tube furnace, where the temperature, pressure, and reacting time were controlled. The samples were heated to a temperature of 550–600 °C for several days in a flow of an oxidizing gas mixture (CO<sub>2</sub>/N<sub>2</sub>/SO<sub>2</sub>, 19.3:80.56:0.14) and H<sub>2</sub>O vapor. Then, they became dark red-brown after the reaction.

The structural and chemical composition of the synthesized product were studied using X-ray diffraction (XRD, Rigaku with Cu K $\alpha$  radiation), scanning electron microscopy (SEM, DB-235 focused ion beam workstation, FEI Company), transmission electron microscopies (TEMs, Tecnai F30, FEI company and Philips CM300 FEG/UT equipped with True-Image professional 1.0.1 software to obtain exit waves), energy-dispersive X-ray spectroscopy (EDX), and electron energy-loss spectroscopy (EELS).

TEM samples were prepared by dispersing the powder in alcohol during ultrasonic treatment. Thereafter, it was dropped onto a porous carbon film supported by a copper grid and dried in air.

## Results and Discussions

The structure of the as-grown samples was first characterized by XRD measurement. Recorded XRD peaks shown in Figure 1a matched the standard hematite sample (Joint Committee on Powder Diffraction Standards Card No. 871164) perfectly, proving that the as-grown products were rhombohedral crystalline hematite ( $\alpha$ -Fe<sub>2</sub>O<sub>3</sub>). Since no peaks from the iron substrate could be observed, the nanowires covered the substrate to a thickness exceeding the X-ray absorption distance of 2–3  $\mu$ m. No additional impurity phase was detected.

\* Authors to whom correspondence should be addressed. E-mail: rmwang@pku.edu.cn; CFKisielowski@lbl.gov.

<sup>†</sup> Peking University.

<sup>‡</sup> University of California.

<sup>§</sup> Present address: School of Science, Beijing University of Aeronautics and Astronautics, Beijing 100083, People's Republic of China.

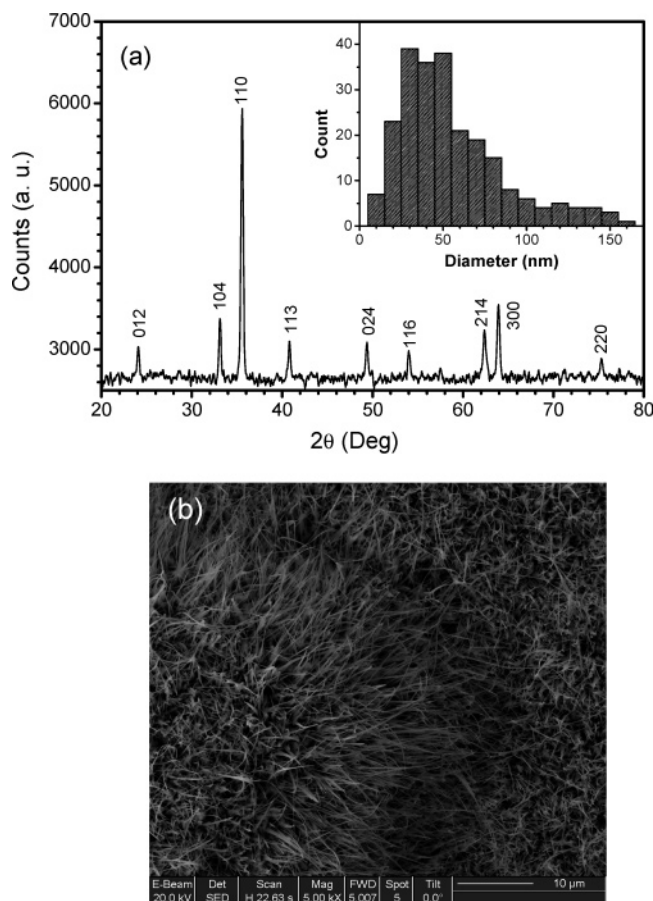


**Figure 1.** Large area of nanoscale nanowires of hematite ( $\alpha$ - $\text{Fe}_2\text{O}_3$ ). (a) XRD pattern recorded from the as-grown nanostructures proves the rhombohedral crystal structure of  $\alpha$ - $\text{Fe}_2\text{O}_3$ . Inset depicts the diameter distribution of the nanowires. (b) Typical SEM image of the synthesized material revealing a large quantity of  $\alpha$ - $\text{Fe}_2\text{O}_3$  nanowires on the iron substrate.

SEM was employed to depict the surface morphology of the sample. Figure 1b shows a typical SEM image of the sample. Large quantities of nanowires were formed on the iron substrates over areas up to several tens of square millimeters. The as-grown nanowires exhibit a uniform diameter with a mean value around 40–50 nm. The diameter distribution extracted from 240 randomly selected individual nanowires is depicted in the inset of Figure 1a. Statistics reveal that over 80% of the nanowires have diameters of 20–80 nm; thereby about half of them have diameters of 30–50 nm. Nanowires with diameters less than 10 nm can be found occasionally. The lengths of these nanowires range from 10 to 20  $\mu\text{m}$  and can be increased with growth time.

Analytical and high-resolution TEM (HRTEM) investigations provide further insight into the structure and the chemical composition of the nanowires. Figures 2a–c show bright-field TEM images of the  $\alpha$ - $\text{Fe}_2\text{O}_3$  nanowires. The nanostructures are generally straight with uniform diameters throughout their length. They can be classified into two types, i.e., single-crystal and bicrystal nanowires. The single-crystal nanowires have the same characteristics as those reported previously.<sup>7</sup> Each of the bicrystal nanowires contains a grain boundary along its entire length in the center as shown in Figure 2. The inset of Figure 2a shows a magnified TEM image from part of the bicrystalline nanowire shown in Figure 2a. The bicrystal nature of the nanowire can be recognized by the alternating bright/dark fringes, which arise from dynamic electron diffraction effects.

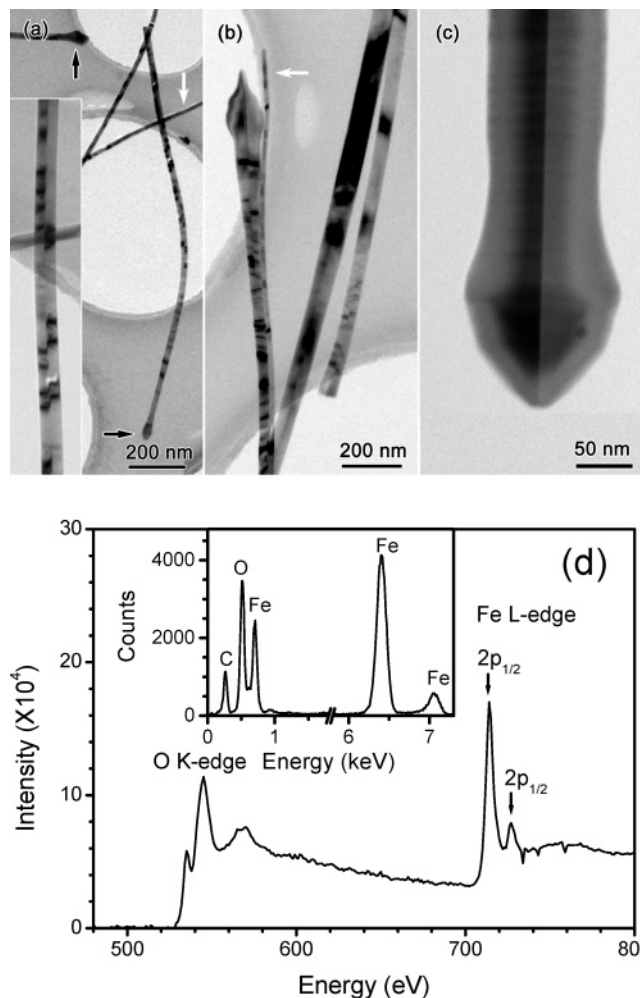


**Figure 2.** Bright-field TEM images and chemical composition of the  $\alpha$ - $\text{Fe}_2\text{O}_3$  bicrystalline nanowires. (a and b) Bright-field TEM images of the  $\alpha$ - $\text{Fe}_2\text{O}_3$  nanowires showing the existence of single-crystal (white arrows) and bicrystal structures. The black arrows point out the ellipsoidal heads of the bicrystalline nanowires. Inset in part a is a magnification, showing the bicrystal nature of the nanowire. (c) Magnified TEM image of a bicrystalline nanowire with an ellipsoidal head, revealing a straight boundary along its whole length. (d) Typical EELS spectrum obtained from one single bicrystalline nanowire, showing characteristic ionization edges of O and Fe. The inset shows the EDX spectrum from the same nanowire.

The nanowires with smaller diameters ( $\leq 50$  nm) tend to form bicrystal structures while those with larger diameters ( $> 50$  nm) tend to have single-crystal structures. Statistics reveal that over 50% of the nanowires are bicrystal nanowires. Thus, it is possible to control the fraction of the bicrystal nanowires by controlling the sizes of the nanowires, which are mainly affected by the reaction gases and temperature.

Investigations also indicate that most of the bicrystalline nanowires have ellipsoidal heads, as marked by arrows in Figure 2a, that are absent from single-crystal nanowires. The diameter of the ellipsoidal head is larger than the diameter of the main body of the bicrystal nanowire. Some of the ellipsoidal heads grow with cone tails, as shown in Figure 1b. The boundary between the two parts of one bicrystalline nanowire extends straight along its entire length including the ellipsoidal head and cone tail if present. The diameters of the tip of the ellipsoidal head and the cone tail are only several nanometers, which may enhance the field-emission property of the hematite nanowires.<sup>8</sup>

Figure 2c shows a magnified bright-field TEM image of a bicrystalline nanowire with an ellipsoidal head. The dark contrast

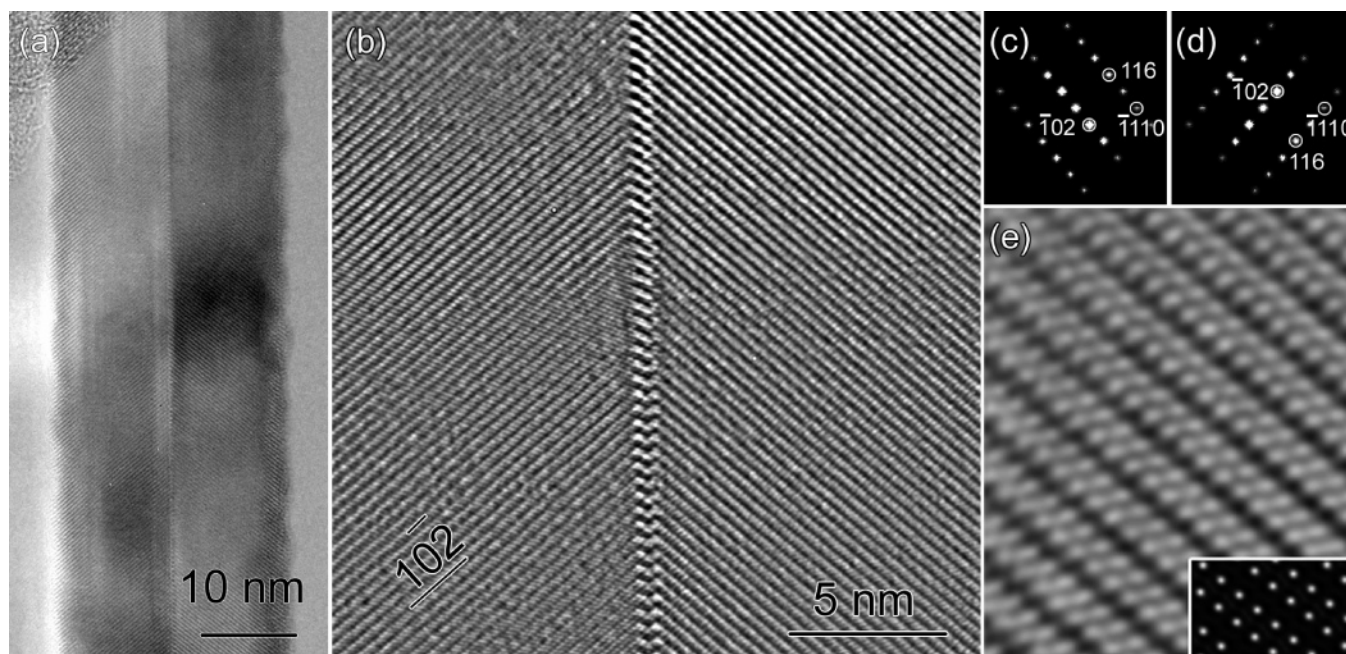


**Figure 3.** HRTEM images of the  $\alpha$ -Fe<sub>2</sub>O<sub>3</sub> bicrystalline nanowires showing a twin structure. (a) HRTEM image of a fine nanowire with a diameter of  $\sim 23$  nm, showing a straight grain boundary at the center of the nanowire. (b) HRTEM image taken from a bicrystal nanowire with diameter of  $\sim 40$  nm, showing a symmetric tilt boundary. (c and d) FFT patterns for both twinning regions in part b. (e) Phase image of the electron exit wave of the  $\alpha$ -Fe<sub>2</sub>O<sub>3</sub> in [281] projection. The inset shows a simulated phase image.

in the center of the head indicates the presence of a different phase, which relates to the growth mechanism of the bicrystalline structure.

A chemical composition analysis of individual nanowires indicates no apparent differences between the single-crystal and the bicrystalline nanowires. Figure 2d shows an EELS spectrum obtained from one single bicrystalline nanowire, exhibiting pronounced peaks at  $\sim 532$  and  $\sim 714$  eV, which correspond to the characteristic K-shell ionization edge of O and the L edge of Fe, respectively. The electron energy-loss near-edge structure of the iron edge in Figure 2d is characteristic for Fe<sup>3+</sup> in  $\alpha$ -Fe<sub>2</sub>O<sub>3</sub>. The separation of the 2p<sub>3/2</sub> and 2p<sub>1/2</sub> energy levels is measured to be 13.2 eV for Fe, which agrees with results from X-ray photoelectron spectroscopy (XPS).<sup>7b</sup> An EDX analysis of the same bicrystalline nanowire is shown in the inset of Figure 2d. The result confirms that the nanowire consists of Fe and O only. It is worth noting that S, N, and C signals from the nanowires are undetectable, although it grows under the atmosphere of CO<sub>2</sub>, N<sub>2</sub>, SO<sub>2</sub>, and H<sub>2</sub>O. The trace sulfur may be segregated at the root of the nanowires.

Figure 3 shows two HRTEM images of the  $\alpha$ -Fe<sub>2</sub>O<sub>3</sub> bicrystalline nanowires. They are taken from a 23 nm narrow nanowire (a) as well as from a wider one (b). Further, the diameters of each of the bicrystal nanowires are constant throughout their whole length except for the ellipsoidal head. Lattice fringes of  $\sim 0.368$  nm spacing corresponding to (10 $\bar{2}$ ) planes of rhombohedral  $\alpha$ -Fe<sub>2</sub>O<sub>3</sub> can be observed on both sides of the boundary in the two HRTEM images. Consequently, both crystal parts form a symmetric tilt boundary. The angle between the (10 $\bar{2}$ ) planes in the two crystals is always  $79.5 \pm 0.5^\circ$  and identical in both images. Selected area diffraction and fast Fourier transformation (FFT) analysis reveal that the incident beam direction is parallel to the [281] direction of the  $\alpha$ -Fe<sub>2</sub>O<sub>3</sub> with rhombohedral structure. The FFT patterns for both twinning regions in Figure 3b are shown in Figures 3c and 3d. The grain boundary is parallel to the ( $\bar{1}10$ ) plane, forming a twin

boundary. Then the orientation relationship between the two sides of the bicrystal nanowire can be described as ( $\bar{1}10$ )<sub>M</sub>//( $\bar{1}10$ )<sub>T</sub>, [281]<sub>M</sub>//[281]<sub>T</sub>, where M and T represent matrix and twin, respectively. The corresponding transformation matrix of the direction indices can be calculated as For another example,

$$\mathbf{B}_1 = \mathbf{B}_1^{-1} = \begin{bmatrix} -0.910 & -0.090 & -0.904 \\ -0.090 & -0.910 & 0.904 \\ -0.182 & 0.182 & 0.819 \end{bmatrix} \quad (1)$$

we find ( $\bar{1}10$ )<sub>M</sub>//(110)<sub>T</sub>, [221]<sub>M</sub>//[110]<sub>T</sub> and the corresponding transformation matrix as

$$\mathbf{B}_2 = \mathbf{B}_2^{-1} = \begin{bmatrix} -0.893 & -0.107 & -0.967 \\ -0.107 & -0.893 & 0.976 \\ -0.196 & 0.196 & 0.785 \end{bmatrix} \quad (2)$$

Considering experimental errors, the two matrixes  $\mathbf{B}_1$  and  $\mathbf{B}_2$  are equivalent. From the matrix  $\mathbf{B}_1$ , we can obtain the crystallographic orientation relationship to be ( $\bar{1}10$ )<sub>M</sub>//( $\bar{1}10$ )<sub>T</sub>, [110]<sub>M</sub>//[110]<sub>T</sub> for the twin boundary. The [110]<sub>M</sub>//[110]<sub>T</sub> orientation relationship of the bicrystalline nanowires is indicative of the relatively higher intensity of (110) reflection in the XRD pattern shown in Figure 1a.

Focal series reconstruction has also been conducted to investigate the atomic structure of the bicrystalline nanostructures. The exit wave phase image reconstructed from 20 lattice images indicates that the interface is slightly declined. A phase image with subangstrom resolution for each crystal part of the nanowire has been obtained, as shown in Figure 3e. The bright contrast corresponds to the atomic position of Fe in the [281] projection. The simulated exit wave phase image using MacTempass software has also been shown in the inset of this reconstructed phase image. The thickness used for the simulation was 40 nm, which is consistent with the diameter of the nanowire.



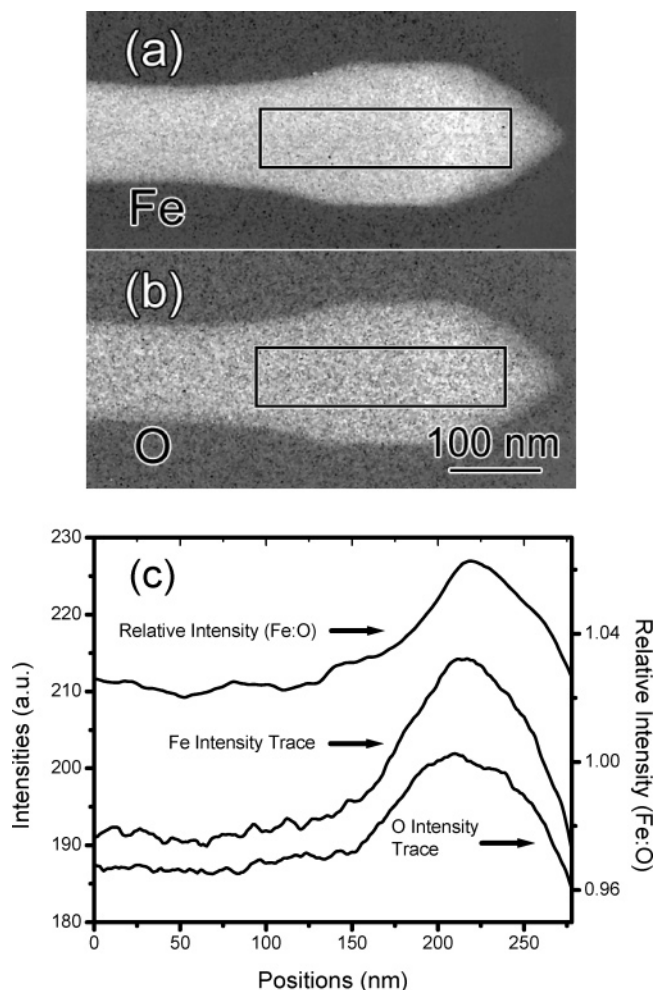
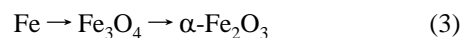


**Figure 4.** EFTEM analysis on the elliptical head from an  $\alpha$ -Fe<sub>2</sub>O<sub>3</sub> bicrystalline nanowire. (a and b) Elemental mapping of iron and oxygen. (c) Line profiles of iron and oxygen signals as well as their ratios across the ellipsoidal head probed along the marked square in parts a and b.

TEM investigations have already demonstrated that the main difference between the single-crystal and bicrystal nanowires lies in their heads. The bicrystalline nanowires always have ellipsoidal heads that are absent from single-crystal nanowires. Therefore, it is essential to investigate the structural and/or compositional difference between the heads and the main body of the nanowire. The interface between the two crystals of the ellipsoidal head has an identical twin structure compared to that of the other part of the nanowire. However, energy-filtered TEM (EFTEM) of the ellipsoidal head indicated that the head is iron-rich. Figures 4a and 4b show the elemental mappings of iron and oxygen, respectively, from the same ellipsoidal head of a typical bicrystalline nanowire. Brighter contrast can be observed in the center of the ellipsoidal head for both iron and oxygen mapping. Line profiles of the intensities of iron and oxygen signals across the ellipsoidal head probed along the marked square in Figures 4a and 4b are depicted Figure 4c. The intensity ratio of Fe/O has also been depicted in Figure 4c. In comparison with the intensity of oxygen, the intensity of the iron line profile around the center of the head is relatively higher. The ratio of Fe/O in the core of the ellipsoidal head about 50 nm in size is higher than that in the straight part of the nanowire, where the ratio of Fe/O remains almost identical. Therefore, the head may be an oxidation precursor of  $\alpha$ -Fe<sub>2</sub>O<sub>3</sub>, similar to the growth of CuO oxidized in air.<sup>6b</sup> Previous work has demonstrated that the

oxidation of iron in air proceeded in the following stages<sup>9</sup>



When iron is oxidized in the mixture of gases including CO<sub>2</sub>, N<sub>2</sub>, SO<sub>2</sub>, and H<sub>2</sub>O, the primary product is Fe<sub>3</sub>O<sub>4</sub>, and then Fe<sub>2</sub>O<sub>3</sub> is formed slowly only through a second step of oxidation. In this case, Fe<sub>3</sub>O<sub>4</sub> served as a precursor to Fe<sub>2</sub>O<sub>3</sub>. The EFTEM analysis of the core of the ellipsoidal head is indicative of the iron-rich Fe<sub>3</sub>O<sub>4</sub> precursor.

Two mechanisms, i.e., the vapor–liquid–solid (VLS)<sup>10</sup> and the vapor–solid (VS),<sup>11</sup> have been commonly used for the growth of nanowires in the gas phase. The VLS mechanism can be first excluded because there are neither catalysts used in our experiments nor particles observed at the top of the obtained nanowires. In our experiments, the evaporation is negligible since the temperature employed is far less than the melting points of iron, Fe<sub>3</sub>O<sub>4</sub>, FeO, and  $\alpha$ -Fe<sub>2</sub>O<sub>3</sub> (1535, 1596, 1370, and 1350 °C, respectively). Moreover, the synthesized nanowires grow directly on the local iron substrate. No different temperature zones are available for the evaporation–condensation process in the experimental conditions. Therefore, the growth of  $\alpha$ -Fe<sub>2</sub>O<sub>3</sub> nanowires is possibly neither a VLS nor a VS process. A solid-phase growth may be introduced to explain the growth mechanism of  $\alpha$ -Fe<sub>2</sub>O<sub>3</sub>, which has been used to interpret the growth of Fe<sub>2</sub>O<sub>3</sub> whiskers.<sup>12</sup> Recently, a similar mechanism has been used to interpret the growth of a GaAs nanowire.<sup>13</sup> The Fe<sub>3</sub>O<sub>4</sub> precursor in the ellipsoidal head is indicative of the tip growth of the  $\alpha$ -Fe<sub>2</sub>O<sub>3</sub> bicrystal nanowires. Neglecting the evaporation process, the supply of the materials for growing  $\alpha$ -Fe<sub>2</sub>O<sub>3</sub> bicrystal nanowires may be surface diffusion and internal diffusion. First, the iron was oxidized into Fe<sub>3</sub>O<sub>4</sub> bicrystalline nanoparticles. Then Fe<sub>2</sub>O<sub>3</sub> nanowires were grown by the surface and internal diffusions.

The growth mechanism may also be applied to most of the other oxide nanowires, such as copper oxide<sup>6b</sup> and tungsten oxide<sup>14</sup> nanowires. In all of the cases, the experimental temperature is far below the melting points of the involved metal and metal oxides, and an oxidation layer grows on the metal substrates. Although it is still unclear whether the nanowires grow on the oxidation layers or stretch out from the layers, our future plan involves a local synthesis of other metal oxide nanowires on the corresponding metal substrates through a direct high-temperature oxidation of metals, where both metal and metal oxides have a relatively high melting point to guarantee a solid-phase growth.

## Conclusions

In summary, we have demonstrated a simple and convenient route to the synthesis of millimeter-sized arrays of  $\alpha$ -Fe<sub>2</sub>O<sub>3</sub> nanowires. Comprehensive TEM investigations indicate that these nanowires with ellipsoidal heads were bicrystalline, with a ( $\bar{1}110$ ) twin plane sitting in the middle of each nanowire along the entire longitudinal axis. The lengths of these nanowires are about 10–20  $\mu$ m, and they can be lengthened with growth time without branching. The ellipsoidal head was found to be iron-rich and is indicative of an Fe<sub>3</sub>O<sub>4</sub> precursor of bicrystalline  $\alpha$ -Fe<sub>2</sub>O<sub>3</sub>. The bicrystalline nanowire grows at the tip by the surface and internal diffusions of molecules from base to tip. The bicrystal structures might have very important roles in the electronic properties of nanowires. They could also serve as templates for novel device structures. The possibility of producing bicrystalline nanowires of other metal oxides using similar methods is also promising.

**Acknowledgment.** This work was partly supported by the National 973 projects (MOST, Grant No. 2002CB613505), the NSFC (Grant No. 10374003), and the Director, Office of Science, Office of Basic Energy Science, of the U. S. Department of Energy under Contract No. DE-AC03-76SF00098. R. M. Wang acknowledges the support from the Berkeley Scholar Program.

**Note Added after ASAP Publication.** This article was published ASAP on June 8, 2005. Part c was added to ref 7. The correct version was reposted on June 23, 2005.

## References and Notes

- (1) (a) Duan, X. F.; Huang, Y.; Cui, Y.; Wang, J. F.; Lieber, C. M. *Nature* **2001**, *409*, 66. (b) Huang, Y.; Duan, X. F.; Wei, Q. Q.; Lieber, C. M. *Science* **2001**, *291*, 630. (c) Xia, Y. N.; Yang, P. D.; Sun, Y. G.; Wu, Y. Y.; Mayers, B.; Gates, B.; Yin, Y. D.; Kim, F.; Yan, Y. Q. *Adv. Mater.* **2003**, *15*, 353. (d) Wang, Z. L. *Adv. Mater.* **2003**, *15*, 432.
- (2) Rao, C. N. R.; Deepak, F. L.; Gautam, G.; Govindaraj, A. *Prog. Solid State Chem.* **2003**, *31*, 5.
- (3) Ohmori, T.; Takahashi, H.; Mametsuka, H.; Suzuki, E. *Phys. Chem. Chem. Phys.* **2000**, *2*, 3519.
- (4) Huo, L.; Li, W.; Lu, L.; Cui, H.; Xi, S.; Wang, J.; Zhao, B.; Shen, Y.; Lu, Z. *Chem. Mater.* **2000**, *12*, 790.
- (5) Geus, J. W. *Appl. Catal.* **1986**, *25*, 313.
- (6) (a) Carim, A. H.; Lew, K. K.; Redwing, J. M. *Adv. Mater.* **2001**, *13*, 1489. (b) Jiang, X. C.; Herricks, T.; Xia, Y. N. *Nano Lett.* **2002**, *2*, 1333. (c) Dai, Y.; Zhang, Y.; Bai, Y. Q.; Wang, Z. L. *Chem. Phys. Lett.* **2003**, *375*, 96. (d) Meng, X. M.; Jiang, Y.; Liu, J.; Lee, C. S.; Bello, I.; Lee, S. T. *Appl. Phys. Lett.* **2003**, *83*, 2244.
- (7) (a) Fu, Y. Y.; Chen, J.; Zhang, H. *Chem. Phys. Lett.* **2001**, *350*, 491. (b) Fu, Y. Y.; Wang, R. M.; Xu, J.; Chen, J.; Yan, Y.; Narlikar, A. V.; Zhang, H. *Chem. Phys. Lett.* **2003**, *379*, 373. (c) Wen, X. G.; Wang, S. H.; Ding, Y.; Wang, Z. L.; Yang, S. H. *J. Phys. Chem. B* **2005**, *109*, 215.
- (8) Zhang, H. Z.; Wang, R. M.; Zhu, Y. W. *J. Appl. Phys.* **2004**, *96*, 624.
- (9) Ren, R. Y.; Yuen, W. Y. D. *Oxid. Met.* **2003**, *59*, 433.
- (10) Morales, A. M.; Lieber, C. M. *Science* **1998**, *279*, 208.
- (11) Shi, W. S.; Zheng, Y. F.; Wang, N.; Lee, C. S.; Lee, S. T. *Chem. Phys. Lett.* **2001**, *345*, 377.
- (12) (a) Tallman, R. L.; Gulbransen, E. A. *Nature* **1968**, *218*, 1046. (b) Gulbransen, E. A.; Copan, T. P.; Anderew, K. F. *Chimia* **1969**, *23*, 472. (c) Takagi, R. *J. Phys. Soc. Jpn.* **1957**, *12*, 1212.
- (13) Persson, A. I.; Larsson, M. W.; Stenstrom, S.; Ohlsson, B. J.; Samuelson, L.; Wallenberg, L. R. *Nat. Mater.* **2004**, *3*, 677.
- (14) Gu, G.; Zheng, B.; Han, W. Q.; Roth, S.; Liu, J. *Nano Lett.* **2002**, *2*, 849.